Surface & Coatings Technology 477 (2024) 130309

Contents lists available at ScienceDirect

Surface & Coatings Technology

journal homepage: www.elsevier.com/locate/surfcoat

Formation of expanded phases in ferritic stainless steel nitrided at low temperatures

Francesca Borgioli

Department of Industrial Engineering (DIEF), University of Florence, via di Santa Marta 3, I-50139 Florence, Italy

ARTICLE INFO

Keywords:
Low-temperature nitriding
Ferritic stainless steel
Expanded ferrite
Expanded ε'-martensite
bcc-to-hcp transformation

ABSTRACT

Nitriding treatments at low temperatures (<450 °C) are receiving increasing interest for the surface engineering of stainless steels due to the possibility of producing supersaturated solid solutions of nitrogen in the iron-based lattices, known as "expanded" phases. In this study this treatment was applied to AISI 430 ferritic stainless steel with the aim of clarifying the characteristics of the modified surface layer, and in particular the microstructure and phase composition. The formation of expanded ferrite caused high compressive stresses, so that local plastic deformation phenomena occurred, observable as microstructural changes (slip lines, grain swelling) both at the surface and in the section of the samples. Moreover, the formation of a nitrogen-containing hexagonal close-packed phase, dissimilar to ε-nitride, was reported for the first time for low-temperature nitrided ferritic stainless steels. It is suggested that this phase might be a N-rich expanded ε'-martensite, which formed from expanded ferrite due to a bcc-to-hcp displacive transformation and it remained in the microstructure owing to the residual compressive stresses and nitrogen and chromium solubilization. The presence of this phase contributed to the increase of surface microhardness together with expanded ferrite. The assessment of the corrosion behaviour in 3.5 wt% NaCl aerated solution by means of electrochemical impedance spectroscopy analysis and potentiodynamic measurements showed that, when the modified surface layer consisted only of expanded ferrite, impedance values and corrosion potential had a marked increase and corrosion current density decreased, as compared to those of the untreated steel, suggesting an enhancement of the resistance to general corrosion. On the contrary, when a heterogeneous modified layer formed (expanded ferrite and N-rich expanded ε'-martensite), a worsening of corrosion resistance was observed.

1. Introduction

Low-temperature thermochemical treatments, performed with nitrogen (N) and/or carbon (C) containing atmospheres, are attractive processes for the surface engineering of stainless steels [1–4]. The use of treatment temperatures, that are lower than those employed for nitriding or carburizing of low alloy steels, allows operating in para-equilibrium conditions [5], in which interstitial atoms can diffuse freely in the alloy while the diffusion of the substitutional atoms is hindered, and thus the precipitation of chromium (Cr) compounds is avoided. As a consequence, supersaturated solid solutions of N and/or C in iron (Fe)-based lattices (ferrite, austenite, martensite), known as "expanded" phases, form, and they enhance surface hardness maintaining or even increasing the corrosion resistance [1–3]. Most research papers devoted to this topic concern the low-temperature thermochemical treatments of austenitic stainless steels and the expanded austenite, which forms in the modified surface layers [1–3,6]. This supersaturated solid solution (up to N ~38 at.% [7], C ~19 at.% [8]) has high hardness values [1,3,6] and very good corrosion resistance [1,6,9,10].

Although ferritic stainless steels have a widespread use, low-temperature treatments of these alloys have received less attention in the international literature [1,3,9]. When the treatments are carried out at temperatures lower than about 450 °C for nitriding and nitrocarburizing [11], or 470 °C for carburizing [5], the precipitation of Cr-based compounds is hindered and expanded ferrite can form. The interstitial atom content in this phase can reach ~24 at.% for N [12] and ~10 at.% for C [5], well above the maximum solubility of these atoms in the body-centred cubic (bcc) lattice of α-Fe (N: 0.4 at.% at 592 °C [13]; C: 0.104 at.% at 727 °C [14]). As a consequence of the bcc lattice expansion, compressive residual stresses develop at the surface [15]. The formation of Fe-based (and, eventually, of Cr-based) compounds (nitrides/carbides) together with expanded ferrite depends on both the treatment conditions (temperature, duration, N and/or C feeding) and

E-mail address: francesca.borgioli@unifi.it.

https://doi.org/10.1016/j.surfcoat.2023.130309
Received 6 November 2023; Received in revised form 7 December 2023; Accepted 12 December 2023
Available online 13 December 2023

steel composition [3]. When nitriding treatments are carried out, the formation of expanded ferrite is competitive to that of the hexagonal close-packed (hcp) ε-$Fe_{2-3}N$ nitride [11,16–20], which tends to form a continuous layer, while few authors reported also the presence of γ′-Fe_4N [17,19] and expanded austenite [21,22]. By changing the nitriding conditions it is possible to obtain a modified surface layer which consists of either expanded ferrite only [11,16], or expanded ferrite and dispersed Fe-based nitrides [16], or a continuous layer of ε-nitride on an inner layer in which expanded ferrite and nitrides are present [18]. Below expanded ferrite, needle-like structures, extending into the substrate, were observed, and they were interpreted as either deformation bands [18] or γ′-Fe_4N precipitates [16,20], although no direct evidence of the formation of this nitride was reported. The presence of an expanded-ferrite layer causes an enhancement of surface hardness up to ~1090 $kg_f\ mm^{-2}$ [16], and a further increase up to ~1200 $kg_f\ mm^{-2}$ when Fe-based nitrides form [17]. When Fe- and Cr-based nitrides form and are a large volume fraction in the modified layer, values as high as 1550 $kg_f\ mm^{-2}$ were reported [11]. Corrosion resistance depends significantly on the microstructure of the modified surface layers. When tested in NaCl solutions, continuous layers consisting of expanded ferrite [9,11,16] or ε-nitride [19] showed an improved corrosion resistance. On the contrary, when the Fe-based nitrides are present as precipitates together with expanded ferrite, microgalvanic effects may occur due to the higher nobility of the nitrides, and corrosion resistance worsens [11,16,19]. Thus, a strict control of the treatment conditions is required, in order to obtain a hardness increase without impairing corrosion resistance, and therefore the studies on the evolution of the modified surface layer are fundamental.

In the present research, the characteristics of the modified surface layer, that was produced in AISI 430 ferritic stainless steel nitrided at low temperatures, were studied in order to investigate their changes as the N content in the modified layer increased. Two different types of plasma treatments were used, a low-pressure fast nitriding treatment, which allowed N enrichment at the surface in a short time, reducing diffusion [23], and a traditional glow-discharge nitriding process [24], which allowed to appreciate the evolution of the modified layers and the eventual occurrence of diffusion-driven transformation phenomena. The treatment conditions (temperature, pressure, duration) were chosen on the basis of literature data [3] in order to hinder Cr nitride precipitation. Microstructure, phase composition and surface microhardness were investigated. Corrosion resistance in 3.5 wt% NaCl solution was evaluated using electrochemical impedance spectroscopy (EIS) analysis and potentiodynamic measurements.

2. Materials and methods

Samples (40 × 17 × 1.9 mm) of AISI 430 ferritic stainless steel were cut from cold rolled, annealed and pickled plates and then ground and polished up to 6-μm diamond suspension. The average chemical composition of the steel was (in wt%): C 0.04, Cr 16.2, Mn 0.33, Si 0.24, S 0.04, P 0.03, Fe bal.

Treatments were performed according to previously described procedures [23,24], using a mixture of 80%$_{vol.}$ N_2 + 20 %$_{vol.}$ H_2. Three different treatment types were employed. Type A and B were low-pressure fast nitriding treatments (130 Pa), which allowed N enrichment at the surface in a short time, reducing diffusion. The treatment procedure was reported in [23]. Briefly, the discharge current density was fixed in two step (first step: 1.9 ± 0.1 mA cm^{-2} up to 115 °C; second step: 2.5 ± 0.1 mA cm^{-2} up to the end of the treatment), while voltage drop and temperature increased freely from the initial conditions (202 ± 5 V; room temperature, 25 °C). At the chosen maximum treatment voltage, the power supply was turned off and the samples cooled down to room temperature under vacuum. For Type-A treatment, a maximum voltage of 645 ± 2 V and a maximum measured temperature of 228 °C were reached (treatment duration: 7 min), while for Type-B treatment the maximum voltage was 655 ± 2 V and the maximum measured temperature was 302 °C (treatment duration: 9 min). Type-C treatment was a glow-discharge nitriding process, as described in [24], consisting of a cathodic sputtering step (pressure 130 Pa), followed by nitriding at 380 °C, 10^3 Pa for 5 h (current density: 1.8 ± 0.1 mA cm^{-2}; voltage drop 155 ± 5 V).

The microstructure of the nitrided samples was examined using optical microscopy and scanning electron microscopy (SEM; Zeiss EVO MA 15) equipped with energy dispersion spectroscopy (EDS) and electron backscatter diffraction (EBSD) system (OXFORD AZTEC 5.0 PS 1). For optical microscopy examination, the usual metallographic techniques were employed. Cross-sections and tapered-sections (5°) of the specimens were obtained. The microstructure was delineated using acetic glyceregia (3 ml HCl, 2 ml HNO_3, 2 ml acetic acid, 1 drop of glycerol). For SEM and EBSD examination, the cross-sectioned specimens were polished up to 1-μm diamond finish, and then vibratory polished using 0.06-μm colloidal silica. For EBSD analysis, data acquisition was performed using an accelerating voltage of 15 kV, a tilt angle of 70°, and the scanning step size ranged from 0.25 to 0.4 μm, depending on magnification. EBSD data were analysed by means of the program ATEX [25].

X-ray diffraction (XRD) analysis (Cu Kα radiation) was carried out (Bruker D8 Advance). The patterns were collected in Bragg-Brentano configuration and they were analysed using the software MAUD [26], which is based on the Rietveld method. By fitting the patterns of the phases present in the depth explored by the X-ray beam, average values of their lattice parameters were estimated, neglecting the effect of local changes in N content and residual stress. Additional diffraction patterns were collected using a constant incident angle, α, of 5, 10 or 15°. Using these conditions, the mean penetration depth (calculated as the depth at which the intensity contribution was 5 % of the intensity diffracted at the surface) ranged from 0.94 μm (α = 5°) to 2.4 μm (α = 15°).

A semi-quantitative evaluation of the elements present at the surface layers was carried out with X-ray fluorescence (XRF) (Rigaku ZSX

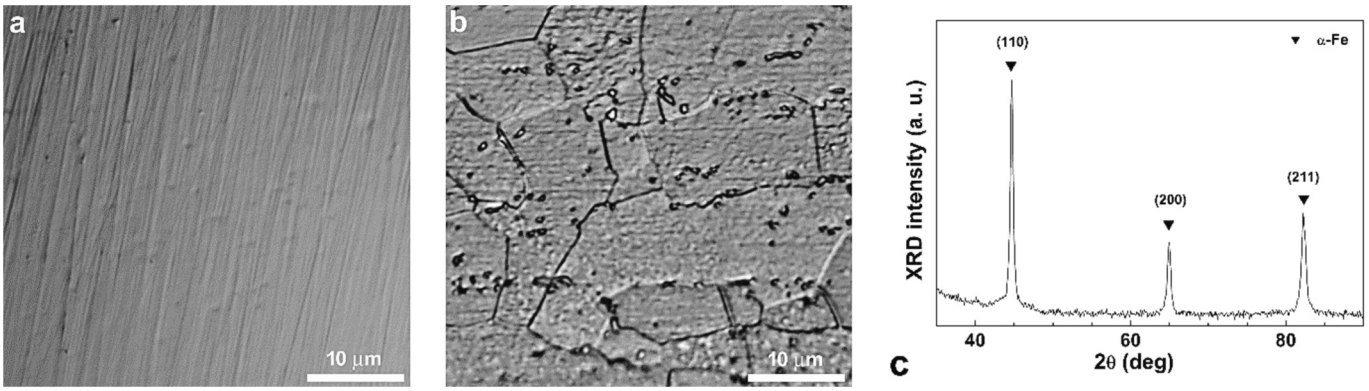

Fig. 1. Surface morphology (a), microstructure (b) (etching: acetic glyceregia) and X-ray diffraction pattern (c) of untreated AISI 430 ferritic stainless steel.

Table 1
Roughness parameters Ra, Rz and Rc for AISI 430 samples untreated and nitrided as indicated.

Sample type	Ra (μm)	Rz (μm)	Rc (μm)
Untreated	0.0059 ± 0.0004	0.046 ± 0.003	0.029 ± 0.002
Type-A nitrided	0.008 ± 0.001	0.055 ± 0.004	0.037 ± 0.004
Type-B nitrided	0.009 ± 0.001	0.075 ± 0.008	0.055 ± 0.008
Type-C nitrided	0.039 ± 0.008	0.33 ± 0.06	0.22 ± 0.05

Primus II).

Roughness was evaluated using a stylus profilometer. The measurements were performed using a 2-μm radius stylus with a 1-mN contact force. The cut-off length was 0.25 mm. The following roughness parameters were measured: the average surface roughness Ra (arithmetical mean deviation of the roughness profile from the mean line), the maximum height of profile Rz (sum of the largest profile peak height and the largest profile valley depth within a sampling length, according to EN-ISO 4287-2009 norm) and the mean height of profile elements Rc (mean value of the profile element heights within a sampling length).

Surface microhardness was measured by means of a Knoop indenter using a load of 10 g_f.

Corrosion resistance was assessed using electrochemical impedance spectroscopy (EIS) analysis and potentiodynamic measurements. The specimens were put in contact with a 3.5 wt% NaCl aerated aqueous solution at room temperature. A three-electrode electrochemical flat cell was used, having an Ag/AgCl reference electrode (3.5 M KCl) and a platinum grid as counter electrode. The sample surface area exposed to the electrolyte was 1 cm^2. All the tests were carried out after 1-h delay. EIS measurements were performed at the open circuit potential (OCP). The frequency range was 10 kHz-10 mHz, with 5 points per decade and an *ac* amplitude (peak-to-peak) of 2.5 mV. EIS spectra were modelled using a nonlinear least square analysis software (EIS Spectrum analyser [27]). Potentiodynamic polarization tests were carried out using a potential scan rate of 0.3 mV s^{-1}. Polarization curves were analysed using the software Gamry Echem Analyst (v. 7.06).

3. Results

3.1. Microstructure

The untreated specimens had a fairly smooth surface, with shallow grooves caused by polishing (Fig. 1a), and a low roughness (Table 1). The microstructure consisted of annealed ferrite grains (Fig. 1b, c). Carbides precipitates were observed, and they were mainly Cr-rich $M_{23}C_6$ (M = Cr, Fe) having a Cr content up to about 68 wt% according to EDS analysis.

The formation of the modified surface layer affected the samples both at the surface (Fig. 2, Table 1) and in the section (Fig. 3).

The surface of Type-A samples, treated up to 228 °C, was slightly etched by ion bombardment and the grain boundaries were faintly delineated, while the grooves due to polishing were still visible (Fig. 2a). A slight increase of surface roughness was registered (Table 1). Thin lines, ascribable to local plastic deformation phenomena, were observed in the tapered-section (Fig. 3a). By performing the EDS analysis on the tapered-section, a N content up to about 4.3 at.% was measured near the surface, higher than the N maximum solubility in α-Fe [13]. In the XRD pattern, collected in Bragg-Brentano configuration, the peaks of ferrite, α-Fe (bcc), present in the substrate, were detected, and they had a small tail at lower diffraction angles, ascribable to expanded ferrite, α_N

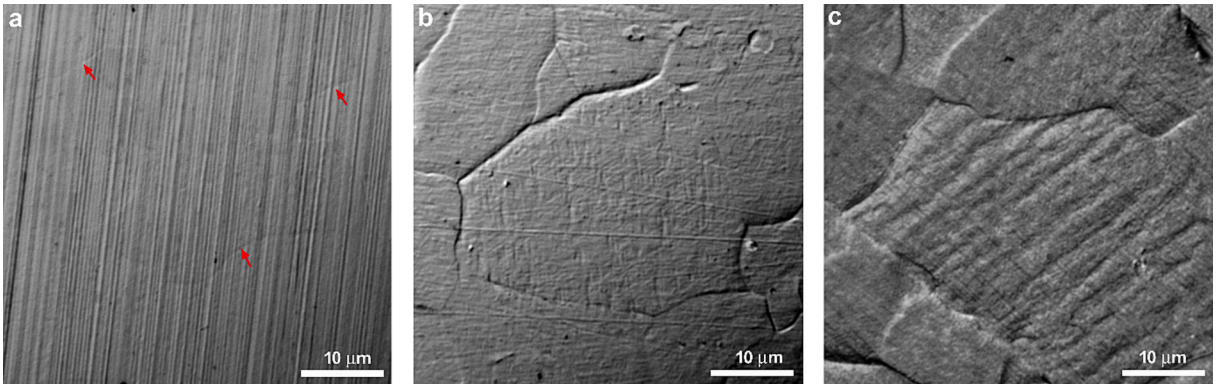

Fig. 2. Surface morphology of Type-A (a), Type-B (b) and Type-C (c) nitrided samples (red arrows in (a) indicate grain boundaries). (For interpretation of the references to color in this figure legend, the reader is referred to the web version of this article.)

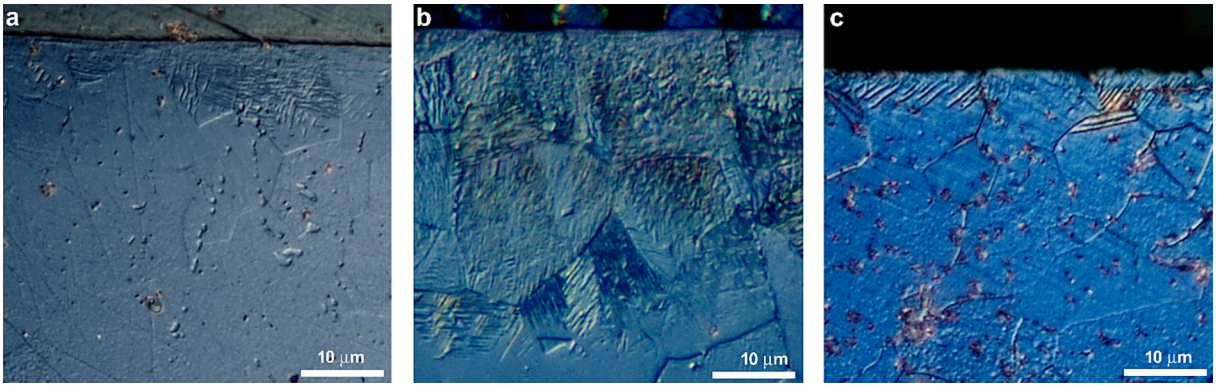

Fig. 3. Micrographs of the 5°-tapered section of Type A (a) and Type-B (b) nitrided samples and of the cross-section of a Type-C (c) nitrided sample (etching: acetic glyceregia) (for (a) and (b) the marker refers to the length in the tapered section).

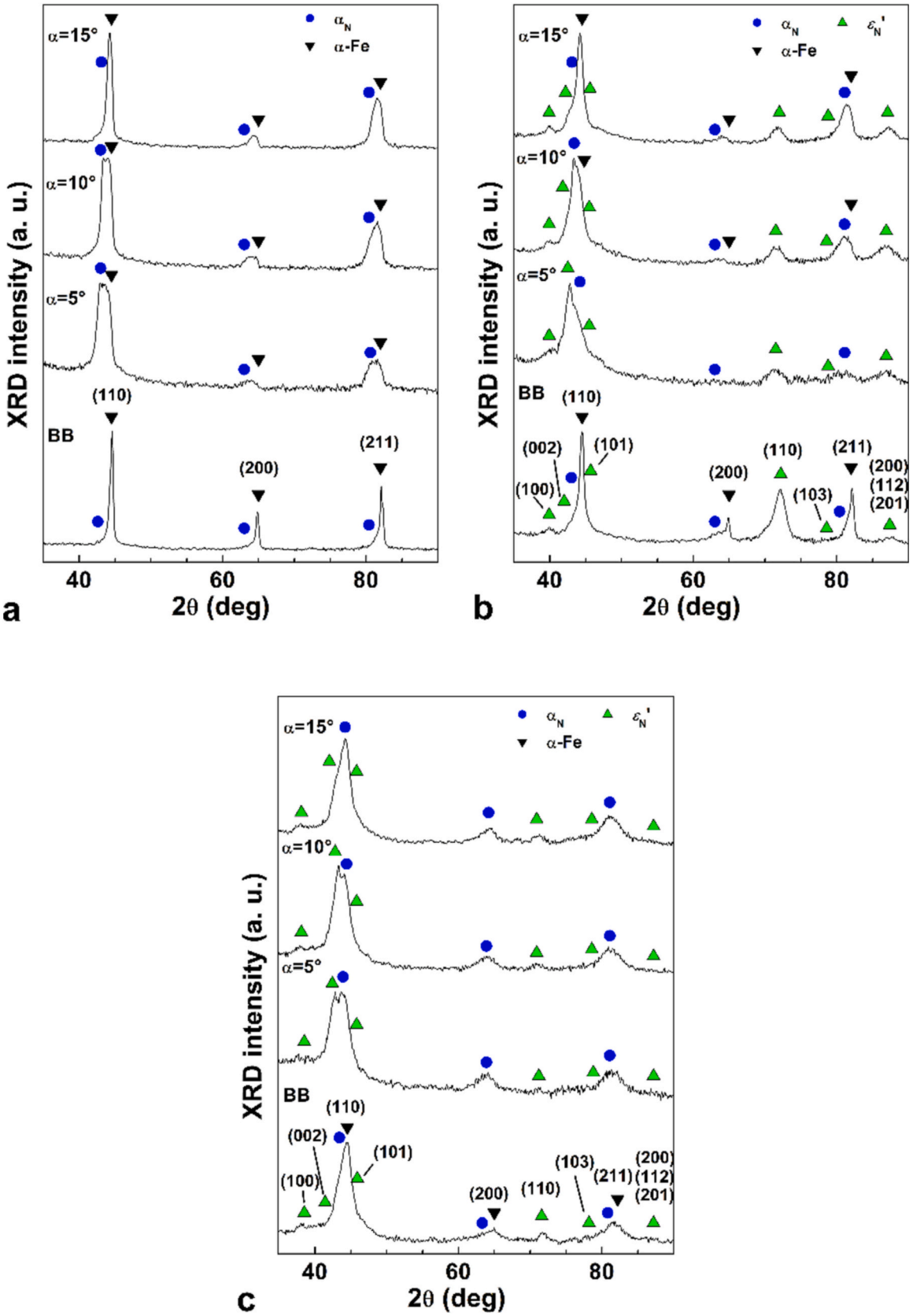

Fig. 4. X-ray diffraction patterns of Type-A (a), Type-B (b) and Type-C (c) nitrided samples (BB: Bragg-Brentano configuration; α: constant incident angle).

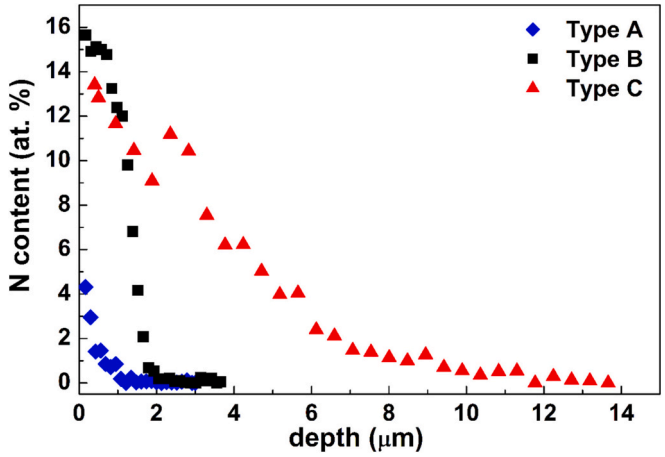

Fig. 5. N content vs depth profile of samples nitrided as indicated.

(Fig. 4a). The presence of this phase is well observable in the patterns collected with constant incident angles. The lattice parameter of α_N was 0.2889 ± 0.0002 nm, significantly higher than that of the ferrite present in the untreated steel (0.2872 ± 0.0001 nm).

When Type-B treatment (nitriding up to 302 °C) was performed, the surface morphology of the samples changed significantly (Fig. 2b). Surface etching due to ion bombardment and nitriding was more marked and the grain boundaries were well delineated. Moreover, lines ascribable to micro-deformation bands, forming chessboard-like regions, were observable within the grains. An increase of surface roughness was registered, especially for Rz and Rc values (Table 1). In the tapered-section slip lines were present, related to extensive plastic deformation phenomena (Fig. 3b). The N content at the surface increased markedly, and values up to about 15.6 at.% were measured by EDS in the tapered-section. In the XRD patterns (Fig. 4b) the peaks of α_N tended to widen and shift towards lower diffraction angles. An increase of the α_N lattice parameter was registered (0.2923 ± 0.0003 nm). Moreover, additional peaks were present. The analysis of peak position suggested that they were due to a phase with a hcp lattice (space group: $P6_3/mmc$), indicated as ε_N' in the figure, having average lattice parameters $a = 0.2621 \pm 0.0002$ nm and $c = 0.4213 \pm 0.0013$ nm. The crystal lattice of this phase was analogous of that of hcp ε'-martensite but with larger lattice parameters [13]. The comparison of ε_N' peak intensities, obtained for Type-B samples in Bragg Brentano configuration, with the powder pattern of this phase, as simulated with the software MAUD, suggested a strong (110) preferred orientation. Fe-based nitrides, γ'-Fe_4N and ε-$Fe_{2-3}N$, and expanded austenite were not detected.

Similar features were observed when Type-C treatment (nitriding at 380 °C) was performed. The surface showed an etched appearance, as that reported for austenitic stainless steels nitrided at low temperature [6] (Fig. 2c). Grain boundaries were well delineated, and grain swelling and grains lining forward on adjacent grains were present. Lines were observable within the grains, suggesting that local plastic deformation phenomena occurred. Surface roughness values increased significantly (Table 1). Analysis of the cross-section showed a surface region faintly etched by chemical etching, which was ascribable to expanded ferrite, as previously reported [17] (Fig. 3c). Many lines, extending from the surface towards the bulk, were also present, similar to the needle-like structures observed by other authors [16,18]. The N content, as measured by EDS analysis in the cross-section, was up to about 13.4 at. %. In the XRD patterns, the peaks of α_N and hcp ε_N' were registered (Fig. 4c), while Fe- and Cr-based nitrides and expanded austenite were not detected. The analysis of XRD patterns obtained with constant incident angles suggested that α_N and ε_N' were present deeper in the uppermost layers of this samples type, if compared to Type-B samples. The lattice parameter of α_N increased slightly, and it was 0.2935 ± 0.0003 nm. A shift of ε_N' peaks towards lower angles was observed for Type-C samples, as compared to Type-B ones, and the estimated lattice parameters for this phase were $a = 0.2628 \pm 0.0002$ nm and $c = 0.4268 \pm 0.0013$ nm.

The N content vs depth profiles were evaluated for all the nitrided samples by means of EDS analysis in the sections, and they are depicted in Fig. 5. For all the samples the profiles were fairly smooth and their trend was similar to the complementary error function, as reported by other authors [5,12]. For Type-A samples a limited N enrichment was observed near the surface. For Type-B samples this N enrichment increased markedly, but the N-rich layer was fairly thin, due to the short treatment duration. For Type-C samples, a thicker N-rich zone was observed. It has to be noted that, for this sample type, the thickness of the N-rich zone was higher than that of the faintly etched zone in Fig. 3c, as previously reported [16]. The thickness of the N-rich layer was ~1 μm for Type-A samples, ~1.9 μm for Type-B samples, and ~10 μm for Type-C samples.

Further EDS analysis was carried out on the section of the samples, in order to put in evidence the eventual formation of N-rich zones which could be ascribed to nitride formation. As an example, the backscattered electron (BSE) image of a Type-C sample is depicted in Fig. 6a, together with N and Cr maps (Fig. 6b and c, respectively). In the N map of all the samples a uniform decrease of the intensity was registered, and neither a continuous nitride layer nor nitride zones were observed. The Cr maps were fairly uniform, and Cr-rich zones were present only where carbides formed.

In order to clarify the nature of the N-rich hcp phase, EBSD analysis was carried out on cross-sectioned samples. When Type-B treatment was performed, in the region near the surface very thin and brighter lines were faintly observable in the forward-scattered electron (FSE) image (Fig. 7a) and a decrease of the band contrast was detected in the image quality (IQ) image (Fig. 7b), in accordance with the presence of local plastic deformations, as observed with optical microscopy analysis. In

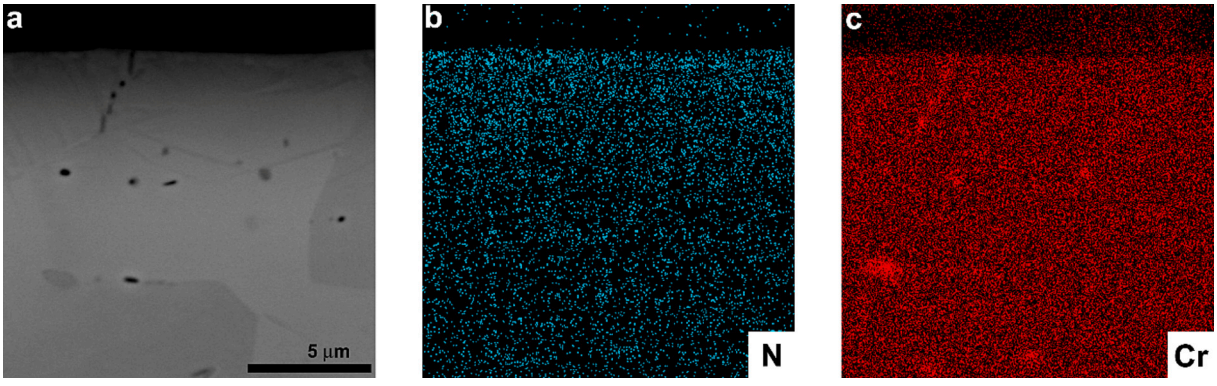

Fig. 6. BSE image (cross-section) (a), N map (b), Cr map (c) for a Type-C nitrided sample.

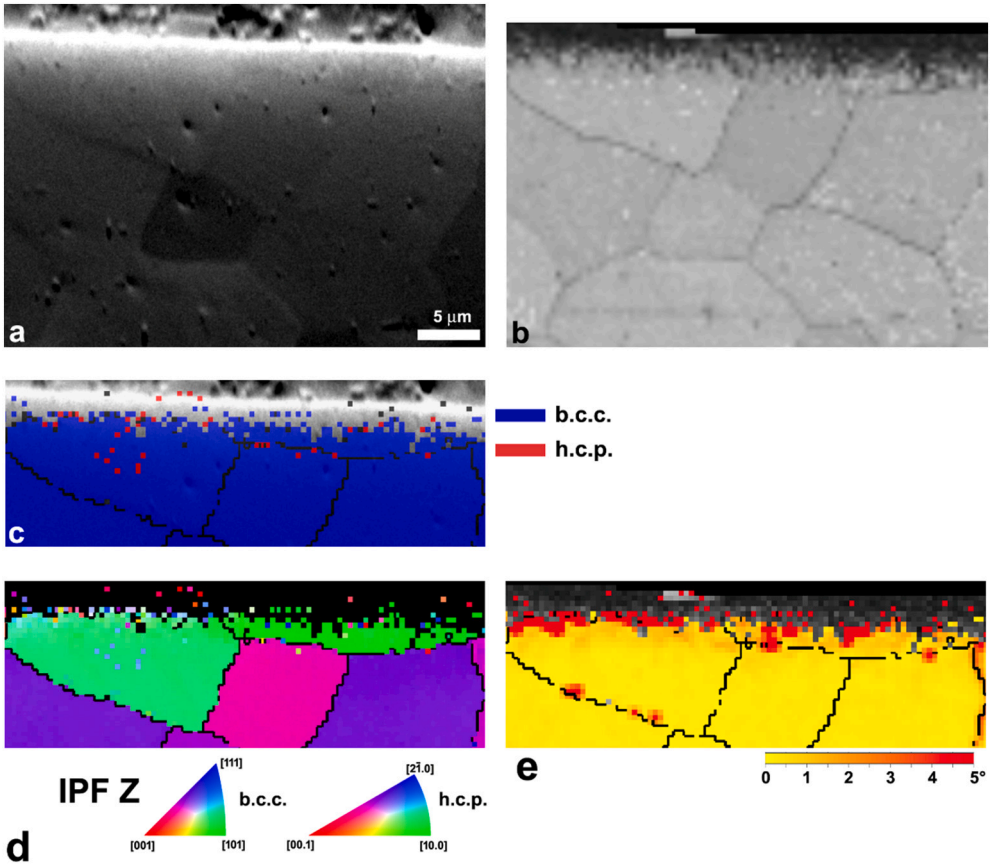

Fig. 7. FSE image (a), IQ image (b), phase composition map (c), IPF map (direction: perpendicular to the observed plane) (d) and KAM map (e) for a Type-B nitrided sample.

this zone the hcp phase was detected (Fig. 7c). According to the inverse pole figure (IPF) (Fig. 7d) and the Kernel Average Misorientation (KAM) map (Fig. 7e), although each grain tended to have a uniform orientation, near the surface a misorientation occurred, probably caused by the plastic deformation phenomena due to expanded ferrite formation. The analysis of Type-C sample allows observing other interesting details of the modified surface layer. The lines extending towards the bulk, detected in Fig. 3c after chemical etching, were clearly observable in the FSE image (Fig. 8a) and in the IQ image (Fig. 8b), even if in this zone the band contrast was poor, suggesting high local plastic deformations. In the phase map the points ascribable to the hcp phase were present in the modified layer and formed irregular stripes, which were parallel to the lines present in the FSE image (Fig. 8c). The presence of γ'-Fe_4N nitride was not detected. The IPF map (Fig. 8d) allowed evaluating the orientation of the observed lines with respect to the ferrite lattice orientation. For the grains A and B, the traces of the {110} planes were depicted on the IQ images. The traces of planes (110) for grain A and of plane $(10\bar{1})$ for grain B, marked in red, were parallel to the observed lines. Using the program ATEX [25], a rough estimate of the Schmid factor was made for assessing the slip systems, which might be active hypothesizing a rotationally symmetric, plane compressive stress [28]. Among the possible slip systems, (110) $[1\bar{1}1]$ for grain A and $(10\bar{1})$ [111] for grain B had high Schmid factor values, so that it can be supposed that the observed lines were indeed slip lines. No twins were detected.

3.2. Surface microhardness

The nitriding treatments increased the surface microhardness of the AISI 430 ferritic stainless steel (Fig. 9). For Type-A samples, the increase was small, due to the fairly low N content of the expanded ferrite and thin thickness of the modified layer. For Type-B samples, higher microhardness values were registered, due to N-richer expanded ferrite, the thicker modified layer, the strain hardening effect caused by local plastic deformations and presumably also to the presence of ε_N'. For Type-C samples, surface microhardness increased further on, due to the further thickness increase of the N-rich modified surface layer.

3.3. Corrosion behaviour

3.3.1. EIS analysis

Representative Bode plots of selected samples, tested in 3.5 wt% NaCl solution, are depicted in Fig. 10. Taking into account the trend of phase angle plots, an equivalent electrical circuit (EEC) with two time constants was chosen for modelling the experimental data. A similar EEC was used for modelling EIS spectra of nitrided austenitic stainless steels [10,29]. The high-frequency time constant is related to charging/discharging at the electrolyte/electrode interface, and the low-frequency time constant to the slower processes in the oxide phase. As depicted in the inset A of Fig. 10 and reported in Table 2, R_s is the resistance of the electrolyte, R_{ct} is the charge transfer resistance, CPE_{dl} is the double layer/space charge capacitance, R_o and CPE_o are related to charge transfer and mass transport in the oxide. The sum of R_{ct} and R_o, R_{tot}, is the polarization resistance and is a measure of the surface total resistance to general corrosion [30]. CPEs represent constant phase elements, which account for surface inhomogeneities, adsorption and diffusion [31]. The impedance of CPE is defined as:

$$Z = [Y\,(i\omega)^n\,]^{-1}$$

where Y is a constant parameter, ω the angular frequency, and n the CPE exponent. A deviation from a pure capacitance behaviour ($n = 1$) was

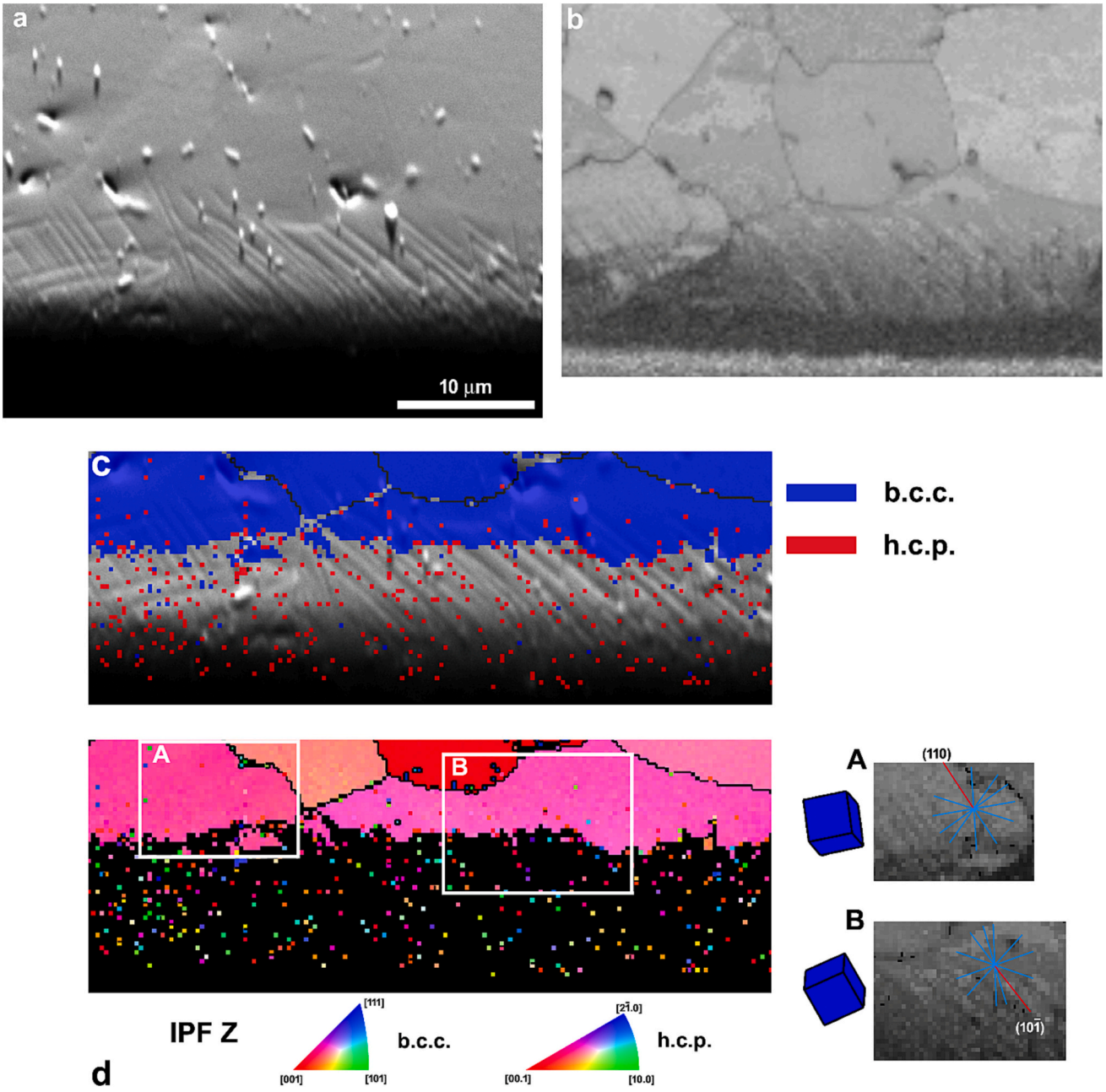

Fig. 8. FSE image (a), IQ image (b), phase composition map (c) and IPF map (direction: perpendicular to the observed plane) (d) for a Type-C nitrided sample. (For inset A and B, {110} plane traces on IQ image and ferrite lattice orientations were depicted.)

observed for all the sample types. The capacitance of the oxide film and of the double layer can be calculated using the formula proposed by Hirschon et al. [32]:

$$C = \left(Y \cdot R^{1-n}\right)^{1/n}$$

The capacitance of the oxide film is inversely proportional to the film thickness, so the higher its value is, the thinner is the passive film [32].

For Type-A samples the impedance and polarization resistance values were markedly higher and the capacitance of the oxide layer was lower as compared to those of the untreated alloy, so it may be hypothesized that the presence of expanded ferrite allowed forming a more protective and thicker oxide layer, which might be able to increase the corrosion resistance. On the contrary, for Type-C samples a decrease of the impedance values and, in particular, of R_o, and an increase of C_o were registered, so it is suggested that a thinner, less protective passive layer formed and the corrosion resistance was expected to decrease.

3.3.2. *Potentiodynamic analysis*

Representative polarization curves of selected samples are depicted in Fig. 11. Corrosion potential, E_{corr}, corrosion current density, i_{corr}, passive current density, i_{pass}, and pitting potential, E_{pit} (evaluated as the potential beyond which anodic current density last crossed 100 μA cm^{-2}), are reported in Table 3. The untreated samples showed a corrosion behaviour typical of a passive material, for which localized corrosion phenomena occur beyond a potential threshold. A similar trend was observed for Type-A nitrided samples, but the corrosion potential was significantly higher and the corrosion current density and the anodic current density values in the passive branch were lower than those of the untreated steel. On the contrary, significant pitting phenomena, which caused a marked increase of anodic current density,

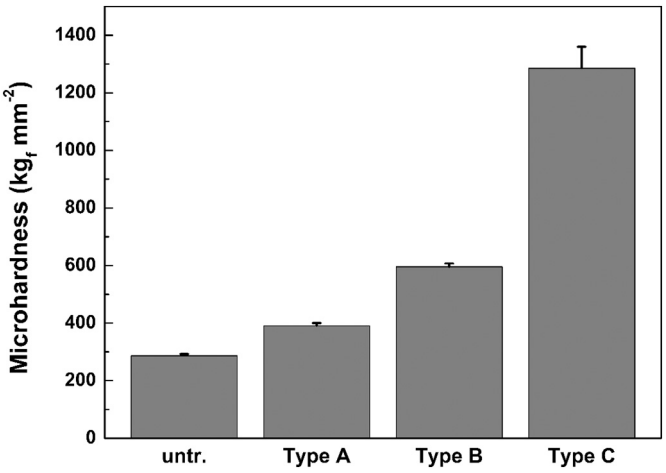

Fig. 9. Surface Knoop microhardness values of samples untreated and nitrided as indicated (load: 10 g_f).

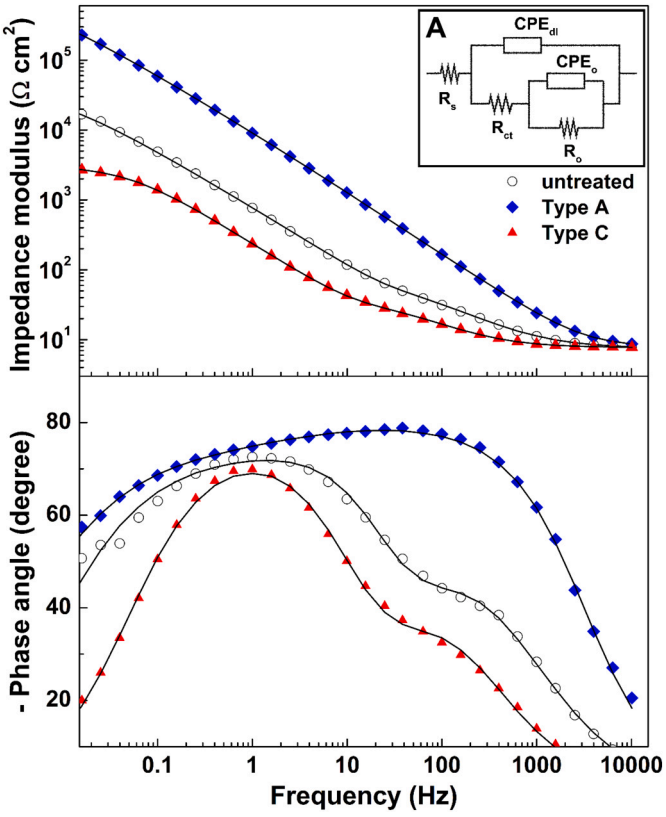

Fig. 10. Bode plots of samples untreated and nitrided as indicated, recorded at the respective OCP values. Symbols: experimental data; lines: modelled data obtained using the equivalent electrical circuit depicted in A as explained in the text (solution: 3.5 wt% NaCl, aerated).

occurred at a lower potential value (E_{pit}) than that registered for the untreated specimens. Regarding Type-C nitrided samples, a significant decrease of corrosion potential and increase of corrosion current density were observed. The trend of the polarization curve was similar to that of a passive material for which an active-passive behaviour happened, but the "passive" branch was very short and had fairly high anodic current values, suggesting that corrosion phenomena were still in progress and a complete repassivation was not possible. After the tests, pit and crevice in correspondence of the PTFE gasket were observable for all the samples types.

4. Discussion

The low-temperature nitriding treatments used in the present study produced modified surface layers, in which expanded ferrite was present without the precipitation of Cr-based nitrides. The different treatment conditions allowed obtaining modified layers having different characteristics. With Type-A treatment, a fairly low N enrichment in a thin layer was produced, and only expanded ferrite was detected. Using Type-B treatment, a higher N content was obtained at the surface, but the short process duration limited diffusion phenomena, and the N-rich modified layer was still fairly thin. With Type-C treatment, the longer process duration allowed N to diffuse further and a thicker N-rich modified surface layer was obtained. As the N content in the layer increased, as in Type-B and -C treatments, together with expanded ferrite a N-rich hcp phase, ε_N', was able to form. The lattice parameters of this phase can be compared with those of the hcp Fe-based ε-nitride, which was usually detected in low-temperature nitrided ferritic stainless steels [11,17–19]. As reported above, for ε_N' a was estimated as 0.2621–0.2628 nm and c as 0.4213–0.4268 nm. For the ε-$Fe_{2\text{-}3}N$ nitride, taking into account the hcp sublattice of Fe atoms, a ranges from 0.2709 to 0.2775 nm and c from 0.4377 to 0.4431 nm, depending on the N content of the nitride [33]. These values were significantly higher than those of ε_N', suggesting that this phase cannot be a N-lean modification of the hcp Fe-based ε-nitride. Microscopy analysis gave further clues on the nature of this phase. According to EDS analysis, no significant change in N content of this phase was detected, if compared to that of expanded ferrite, so ε_N' could not be distinguished on the basis of chemical composition. Similarly, metallographic analysis did not delineate a separate layer which might be ascribed to this phase, and only lines related to plastic deformation phenomena were visible. The results of EBSD analysis pointed out that this phase also formed in the inner part of the modified surface layer and it was related to the slip lines produced in the expanded ferrite grains. Moreover, it has to be noted that this phase was able to form in the fairly fast Type-B nitriding treatment, but it was not significantly affected by the longer treatment duration of Type-C nitriding, so that it might be supposed that it was not formed from a diffusion-driven transformation. Thus, on the basis of the experimental results as a whole it may be suggested that this phase might be analogous to the N-rich deformation-induced hcp ε'-martensite, ε_N', observable in low-temperature nitrided austenitic stainless steels [3,6,24,34–36], and it formed from expanded ferrite owing to the compressive stresses which developed as a consequence of the huge N solubilization in the ferrite lattice. To the best of our knowledge, it is the first study that reports the formation of this "expanded" ε'-martensite in low-temperature nitrided ferritic stainless steels. In pure iron, bcc-to-hcp martensitic transformation was reported to occur when high static or dynamic compressive stresses were applied [37–41]. Very high stress, 14–15 GPa, was required to start the transformation at room temperature [37–39], while a decrease of the needed pressure up to 4.1 GPa was reported as temperature increased up to 297 °C [39]. A decrease of the transformation pressure was observed also when Fe was alloyed with Cr, suggesting that this element tended to stabilize the hcp phase [42]. The lattice parameters of ε'-martensite were reported to be $a = 0.2485$ nm, $c = 0.3990$ nm [13], smaller than that of ε_N', in accordance with the fact that N was solubilized in ε_N'. The bcc-to-hcp transformation is reversible, and hence in pure Fe the presence of ε'-martensite was usually detected by means of in situ measurements during compressive stresses [37–39], or afterwards by indirect observation of the changes in the ferrite microstructure with the formation of twins [40,41]. It may be hypothesized that the presence of compressive residual stresses in the modified surface layer might maintain ε_N' and hinder the reverse transformation (hcp-to-bcc), observed in pure iron [37,38,40,41]. However, taking into account that residual stresses decreased gradually in the inner part of the modified layer, where EBSD

Table 2
Best fitting EEC parameter values for EIS spectra of untreated and nitrided AISI 430 samples tested in aerated 3.5 % NaCl at the respective OCP (model: see inset A in Fig. 10).

Sample type	R_s (Ω cm^2)	R_{ct} (kΩ cm^2)	$Y_{dl} \times 10^5$ (Ω^{-1} s^n cm^{-2})	n_{dl}	R_o (kΩ cm^2)	$Y_o \times 10^5$ (Ω^{-1} s^n cm^{-2})	n_o	R_{tot} (kΩ cm^2)	C_{dl} (μF cm^{-2})	C_o (μF cm^{-2})
Untreated	7.6 ± 0.1	0.11 ± 0.02	12 ± 4	0.81 ± 0.02	43 ± 4	7 ± 1	0.92 ± 0.02	43 ± 4	41 ± 8	82 ± 20
Type-A nitrided	7.7 ± 0.1	87 ± 16	2.2 ± 0.2	0.88 ± 0.01	515 ± 100	0.95 ± 0.03	0.70 ± 0.02	602 ± 101	24 ± 2	18 ± 3
Type-C nitrided	7.6 ± 0.1	0.05 ± 0.01	43 ± 9	0.77 ± 0.1	3.1 ± 0.1	27 ± 10	0.95 ± 0.02	3.2 ± 0.1	138 ± 23	272 ± 12

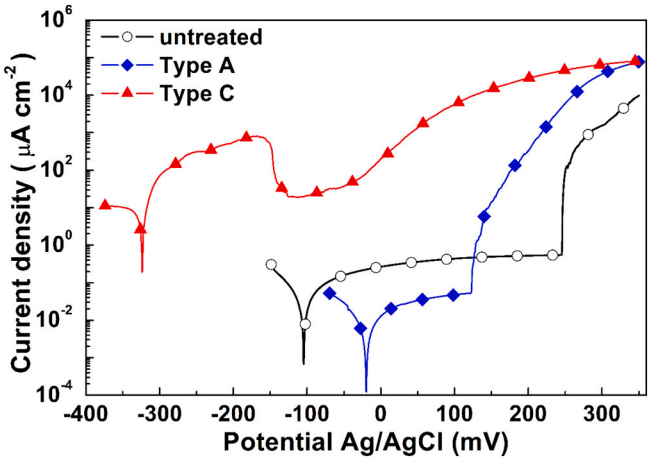

Fig. 11. Polarization curves of samples untreated and nitrided as indicated (solution: 3.5 wt% NaCl, aerated).

Table 3
Corrosion potential, E_{corr}, corrosion current density, i_{corr}, passive current density, i_{pass}, and pitting potential, E_{pit} (evaluated as the potential beyond which anodic current density last crossed 100 μA cm^{-2}), of untreated and nitrided AISI 430 samples (solution: 3.5 wt% NaCl, aerated).

Sample type	E_{corr} (mV (Ag/AgCl))	i_{corr} (μA cm^{-2})	i_{pass} (μA cm^{-2})	E_{pit} (mV (Ag/AgCl))
Untreated	−105 ± 10	0.13 ± 0.01	0.44 ± 0.09	+250 ± 10
Type-A nitrided	−19 ± 10	0.04 ± 0.01	0.044 ± 0.006	+177 ± 10
Type-C nitrided	−323 ± 10	10.2 ± 0.1	25 ± 5	−15 ± 10

analysis evidenced that hcp phase was still present, it may be supposed that both Cr and N also played a role in maintaining this phase, as in austenitic stainless steels [3,6,24].

Thus, the obtained results suggest that the formation of the modified surface layer in ferritic stainless steels was similar to that in austenitic stainless steels [1,6,28]. As N was solubilized, the lattice expansion of ferrite grains in the zone near the surface was constrained by the neighbours and internal compressive stresses developed. These stresses were not accommodated only elastically, and local plastic deformation phenomena might occur, observable both at the surface (slip lines, grain swelling) and in the section (slip lines). As a consequence, compressive residual stresses were present [15]. When a fairly low N amount was solubilized, as for Type-A samples, expanded ferrite formed, but local plastic deformations were limited and expanded martensite was not detectable. As the N content in the surface layers increased significantly and a N-richer expanded ferrite formed, as for Type-B and -C samples, compressive stresses increased and extensive plastic deformation phenomena occurred, promoting the formation of a N-rich stress-induced hcp expanded ε'-martensite, ε_N', from the expanded ferrite. Moreover, ε_N' might promote the formation of hcp ε-$Fe_{2\text{-}3}N$ nitride, as it occurs in austenitic stainless steels [35], and hence influence ε-nitride distribution in the modified surface layer.

It has to be noted that, while the formation of ε-nitride in low-temperature nitrided ferritic stainless steels was reported by many authors [11,17–19], the formation of expanded martensite was not reported before. Taking into account the treatment conditions used in the present study, it may be hypothesized that they allowed a N enrichment which was able to promote plastic deformation phenomena, and thus the formation of expanded ε'-martensite, instead of the formation of nitrides. However, it is possible that expanded martensite formed also in nitrided samples reported in literature, but it was not recognized or it evolved into the observed N-richer ε-nitride.

The presence of ε_N' contributed to increase the surface hardness together with expanded ferrite and the strain hardening effect caused by local plastic deformations. On the contrary, its formation seemed to have a deleterious effect on the corrosion resistance in NaCl solution. The results of EIS analysis and potentiodynamic measurements suggested that, when only expanded ferrite formed, as for Type-A nitrided samples, an increase of the protectiveness of the passive layer might occur, in accordance with higher values of impedance and corrosion potential and lower values of corrosion current density and anodic current density in the passive branch. However, the small thickness of the nitrided layer and the fairly low N content in α_N were not able to counteract totally the localized corrosion phenomena as the polarization potential values increased. A similar behaviour was observed for low-temperature nitrided austenitic stainless steels, for which a significant increase of the resistance to localized corrosion was observed only when fairly thick modified layers consisting of N-rich expanded austenite were produced [10,23,43,44]. When ε_N' formed together with expanded ferrite, as for Type-C samples, the corrosion resistance decreased significantly, as shown by the marked decrease of impedance values and corrosion potential and increase of corrosion current density. It may be hypothesized that the heterogeneous microstructure consisting of expanded ferrite and expanded ε'-martensite was not able to form a highly protective passive layer, so that corrosion phenomena might easily occur. It has to be noted that this behaviour was dissimilar from that observed in nitrided austenitic stainless steels, for which the formation of N-rich ε_N' with expanded austenite did not significantly impair the corrosion resistance in NaCl solutions [10,45,46]. Thus, the nitriding conditions of ferritic stainless steels have to be controlled for reducing local plastic deformation phenomena, and hence hindering the formation of the expanded ε'-martensite, when corrosion resistance in NaCl is a major concern.

5. Conclusions

On the basis of the experimental results the following main conclusions can be drawn.

- Using low-temperature nitriding treatments on ferritic stainless steels modified surface layers were produced, in which N was

solubilized in ferrite well beyond the solubility limit, so that the so called expanded ferrite could form.
- The solubilization of a high nitrogen content in the ferrite caused an expansion of the bcc lattice, which was also accommodated by local plastic deformations. As a consequence of these plastic deformations, a N-containing hcp phase formed, dissimilar to ε-nitride. It is suggested that this phase, which has been indicated as expanded ε'-martensite, is analogous to the deformation-induced N-rich ε'-martensite, which formed in nitrided austenitic stainless steels.
- The modified surface layers, consisting of either expanded ferrite only or expanded ferrite with expanded ε'-martensite, increased surface hardness.
- When only expanded ferrite was formed, an increase of impedance values and corrosion potential, and a decrease of corrosion current density were observed in 3.5 wt% NaCl aerated solution, suggesting a higher resistance to general corrosion. However, the fairly low N content in expanded ferrite and the small thickness of the modified layer did not allow to enhance the resistance to localized corrosion phenomena for the samples examined in the present study.
- When both expanded ferrite and expanded ε'-martensite were present in the modified layer, a significant decrease of the impedance values and corrosion potential, and a marked increase of corrosion current density were registered, and hence a worsen of corrosion resistance in NaCl solution was expected.

CRediT authorship contribution statement

Francesca Borgioli: Conceptualization, Data curation, Formal analysis, Funding acquisition, Investigation, Methodology, Project administration, Supervision, Writing – original draft, Writing – review & editing.

Declaration of competing interest

The author declares that she has no known competing financial interests or personal relationships that could have appeared to influence the work reported in this paper.

Data availability

Data will be made available on request.

Acknowledgements

Technical assistance of Dr. L. Chiarantini and Dr. T. Catelani (Centro di Microscopia Elettronica e Microanalisi – MEMA, University of Florence), for SEM and EBSD measurements, and of Dr. S. Ciattini, Dr. L. Chelazzi and Dr. E. Fantechi (Centro di Cristallografia Strutturale – CRIST, University of Florence), for XRD and XRF measurements, is gratefully acknowledged.

Funding

This work was supported by MUR (Ministero dell'Università e della Ricerca) (years 2022, 2023).

References

[1] H. Dong, S-phase surface engineering of Fe-Cr, Co-Cr and Ni-Cr alloys, Int. Mater. Rev. 55 (2010) 65–98, https://doi.org/10.1179/095066009X12572530170589.
[2] R.P. Cardoso, M. Mafra, S.F. Brunatto, Low-temperature thermochemical treatments of stainless steels – an introduction, in: T. Mieso (Ed.), Plasma Sci. Technol. - Prog. Phys. States Chem. React, InTech, Rijeka, Croatia, 2016, pp. 107–130, https://doi.org/10.5772/61989.
[3] F. Borgioli, The "expanded" phases in the low-temperature treated stainless steels: a review, Metals 12 (2022) 331, https://doi.org/10.3390/met12020331.
[4] M.A.J. Somers, T.L. Christiansen, Low temperature surface hardening of stainless steel, in: E.J. Mittemeijer, M.A.J. Somers (Eds.), Thermochem. Surf. Eng. Steels, Woodhead Publishing, Oxford, UK, 2015, pp. 557–579, https://doi.org/10.1533/9780857096524.4.557.
[5] G.M. Michal, X. Gu, W.D. Jennings, H. Kahn, F. Ernst, A.H. Heuer, Paraequilibrium carburization of duplex and ferritic stainless steels, Metall. Mater. Trans. A 40 (2009) 1781–1790, https://doi.org/10.1007/s11661-009-9826-0.
[6] F. Borgioli, From austenitic stainless steel to expanded austenite-S phase: formation, characteristics and properties of an elusive metastable phase, Metals 10 (2020) 187, https://doi.org/10.3390/met10020187.
[7] T. Christiansen, M.A.J. Somers, Controlled dissolution of colossal quantities of nitrogen in stainless steel, Metall. Mater. Trans. A 37 (2006) 675–682, https://doi.org/10.1007/s11661-006-0039-5.
[8] T.L. Christiansen, K. Ståhl, B.K. Brink, M.A.J. Somers, On the carbon solubility in expanded austenite and formation of Hägg carbide in AISI 316 stainless steel, Steel Res. Int. 87 (2016) 1395–1405, https://doi.org/10.1002/srin.201500415.
[9] H.-J. Spies, Corrosion behaviour of nitrided, nitrocarburised and carburised steels, in: E.J. Mittemeijer, M.A.J. Somers (Eds.), Thermochem. Surf. Eng. Steel, Woodhead Publishing, Oxford, 2015, pp. 267–309, https://doi.org/10.1533/9780857096524.2.267.
[10] F. Borgioli, The corrosion behavior in different environments of austenitic stainless steels subjected to thermochemical surface treatments at low temperatures: an overview, Metals 13 (2023) 776, https://doi.org/10.3390/met13040776.
[11] J. Alphonsa, S. Mukherjee, V.S. Raja, Study of plasma nitriding and nitrocarburising of AISI 430F stainless steel for high hardness and corrosion resistance, Corros. Eng. Sci. Technol. 53 (2018) 51–58, https://doi.org/10.1080/1478422X.2017.1396648.
[12] D. Manova, G. Thorwarth, S. Mändl, H. Neumann, B. Stritzker, B. Rauschenbach, Variable lattice expansion in martensitic stainless steel after nitrogen ion implantation, Nucl. Instruments Methods Phys. Res. Sect. B 242 (2006) 285–288, https://doi.org/10.1016/j.nimb.2005.08.059.
[13] H.A. Wriedt, N.A. Gokcen, R.H. Nafziger, The Fe-N (iron-nitrogen) system, Bull. Alloy Phase Diagr. 8 (1987) 355–377, https://doi.org/10.1007/BF02869273.
[14] H. Okamoto, The C-Fe (carbon-iron) system, J. Phase Equilibria 13 (1992) 543–565, https://doi.org/10.1007/BF02665767.
[15] L.C. Gontijo, R. Machado, L.C. Casteletti, S.E. Kuri, P.A.P. Nascente, X-ray diffraction characterisation of expanded austenite and ferrite in plasma nitrided stainless steels, Surf. Eng. 26 (2010) 265–270, https://doi.org/10.1179/026708410X12550773057983.
[16] B.C.E. Schibicheski Kurelo, G.B. de Souza, F.C. Serbena, C.M. Lepienski, P. C. Borges, Mechanical properties and corrosion resistance of α_N-rich layers produced by PIII on a super ferritic stainless steel, Surf. Coat. Technol. 403 (2020), 126388, https://doi.org/10.1016/j.surfcoat.2020.126388.
[17] L.A. Luiz, B.C.E.S. Kurelo, G.B. de Souza, J. de Andrade, C.E.B. Marino, Effect of nitrogen plasma immersion ion implantation on the corrosion protection mechanisms of different stainless steels, Mater. Today Commun. 28 (2021), 102655, https://doi.org/10.1016/j.mtcomm.2021.102655.
[18] B. Larisch, U. Brusky, H.-J. Spies, Plasma nitriding of stainless steels at low temperatures, Surf. Coat. Technol. 116-119 (1999) 205–211, https://doi.org/10.1016/S0257-8972(99)00084-5.
[19] L. Li, R. Liu, Q. Liu, Z. Wu, X. Meng, Y. Fang, Effects of initial microstructure on the low-temperature plasma nitriding of ferritic stainless steel, Coatings 12 (2022) 1404, https://doi.org/10.3390/coatings12101404.
[20] S. Hamashima, A. Nishimoto, Thickening of S-phase and Sα-phase of various stainless steels treated by low temperature plasma nitriding using screen, Mater. Trans. 63 (2022) 1170–1178, https://doi.org/10.2320/matertrans.MT-M2022062.
[21] Y. Jirásková, C. Blawert, O. Schneeweiss, Thermal stability of stainless steel surfaces nitrided by plasma immersion ion implantation, Phys. Status Solidi 175 (1999) 537–548, https://doi.org/10.1002/(SICI)1521-396X(199910)175:2<537::AID-PSSA537>3.0.CO;2-B.
[22] B.C.E. Schibicheski Kurelo, C.M. Lepienski, W.R. de Oliveira, G.B. de Souza, F. C. Serbena, R.P. Cardoso, J.C.K. das Neves, P.C. Borges, Identification of expanded austenite in nitrogen-implanted ferritic steel through in situ synchrotron X-ray diffraction analyses, Metals 13 (2023), 1744, https://doi.org/10.3390/met13101744.
[23] F. Borgioli, E. Galvanetto, T. Bacci, Surface modification of austenitic stainless steel by means of low pressure glow-discharge treatments with nitrogen, Coatings 9 (2019) 604, https://doi.org/10.3390/coatings9100604.
[24] F. Borgioli, E. Galvanetto, T. Bacci, Low temperature nitriding of AISI 300 and 200 series austenitic stainless steels, Vacuum 127 (2016) 51–60, https://doi.org/10.1016/j.vacuum.2016.02.009.
[25] B. Beausir, J.-J. Fundenberger, Analysis tools for electron and X-ray diffraction, ATEX-software, Université de Lorraine - Metz, 2017. www.atex-software.eu.
[26] L. Lutterotti, S. Matthies, H.-R. Wenk, MAUD (material analysis using diffraction): a user friendly Java program for Rietveld texture analysis and more, in: J. A. Szpunar (Ed.), Proceeding 12th Int. Conf. Textures Mater, NRC Research Press, Ottawa, 1999, pp. 1599–1604.
[27] A.S. Bondarenko, G.A. Ragoisha, Inverse problem in potentiodynamic electrochemical impedance, in: A.L. Pomerantsev (Ed.), Prog. Chemom. Res, Nova Science Publishers, Inc., New York, 2005, pp. 89–102.
[28] M. Somers, Ö. Kücükyildiz, C. Ormstrup, H. Alimadadi, J. Hattel, T. Christiansen, G. Winther, Residual stress in expanded austenite on stainless steel; origin, measurement, and prediction, Mater. Perform. Charact. 7 (2018) 693–716, https://doi.org/10.1520/MPC20170145.
[29] F. Borgioli, E. Galvanetto, T. Bacci, Corrosion behaviour of low temperature nitrided nickel-free, AISI 200 and AISI 300 series austenitic stainless steels in NaCl solution, Corros. Sci. 136 (2018) 352–365, https://doi.org/10.1016/j.corsci.2018.03.026.

[30] Z. Bou-Saleh, A. Shahryari, S. Omanovic, Enhancement of corrosion resistance of a biomedical grade 316LVM stainless steel by potentiodynamic cyclic polarization, Thin Solid Films 515 (2007) 4727–4737, https://doi.org/10.1016/j.tsf.2006.11.054.
[31] S. Omanovic, S.G. Roscoe, Electrochemical studies of the adsorption behavior of bovine serum albumin on stainless steel, Langmuir 15 (1999) 8315–8321, https://doi.org/10.1021/la990474f.
[32] B. Hirschorn, M.E. Orazem, B. Tribollet, V. Vivier, I. Frateur, M. Musiani, Determination of effective capacitance and film thickness from constant-phase-element parameters, Electrochim. Acta 55 (2010) 6218–6227, https://doi.org/10.1016/j.electacta.2009.10.065.
[33] M.A.J. Somers, B.J. Kooi, L. Maldzinski, E.J. Mittemeijer, A.A. Van Der Horst, A. M. Van Der Kraan, N.M. Van Der Pers, Thermodynamics and long-range order of interstitials in an h.c.p. lattice: nitrogen in ε-Fe_2N_{1-z}, Acta Mater. 45 (1997) 2013–2025, https://doi.org/10.1016/S1359-6454(96)00307-2.
[34] M.K. Lei, Phase transformations in plasma source ion nitrided austenitic stainless steel at low temperature, J. Mater. Sci. 34 (1999) 5975–5982, https://doi.org/10.1023/A:1004728711459.
[35] M.K. Lei, Y. Huang, Z.L. Zhang, In situ transformation of nitrogen-induced h.c.p. martensite in plasma source ion–nitrided austenitic stainless steel, J. Mater. Sci. Lett. 17 (1998) 1165–1167, https://doi.org/10.1023/A:1006552618285.
[36] X. Tao, J. Qi, M. Rainforth, A. Matthews, A. Leyland, On the interstitial induced lattice inhomogeneities in nitrogen-expanded austenite, Scr. Mater. 185 (2020) 146–151, https://doi.org/10.1016/j.scriptamat.2020.04.045.
[37] A. Dewaele, C. Denoual, S. Anzellini, F. Occelli, M. Mezouar, P. Cordier, S. Merkel, M. Véron, E. Rausch, Mechanism of the α-ε phase transformation in iron, Phys. Rev. B 91 (2015), 174105, https://doi.org/10.1103/PhysRevB.91.174105.
[38] S. Merkel, A. Lincot, S. Petitgirard, Microstructural effects and mechanism of bcc-hcp-bcc transformations in polycrystalline iron, Phys. Rev. B 102 (2020), 104103, https://doi.org/10.1103/PhysRevB.102.104103.
[39] S. Merkel, H.-P. Liermann, L. Miyagi, H.-R. Wenk, In situ radial X-ray diffraction study of texture and stress during phase transformations in bcc-, fcc- and hcp-iron up to 36GPa and 1000K, Acta Mater. 61 (2013) 5144–5151, https://doi.org/10.1016/j.actamat.2013.04.068.
[40] J. Hu, X. Liu, T. Mashimo, J. Zhang, G. Luo, Y. Sun, Q. Shen, H. Huang, L. Zhang, Experimental and atomic observations of phase transformations in shock-compressed single-crystal Fe, Materialia 20 (2021), 101200, https://doi.org/10.1016/j.mtla.2021.101200.
[41] M. Yu, Z. Guo, X. Meng, Y. Chen, J. Yu, M. Sui, Direct approaches to distinguishing deformation and phase transformation structures in shock-loaded iron, Mater. Charact. 194 (2022), 112436, https://doi.org/10.1016/j.matchar.2022.112436.
[42] K. Ishida, T. Nishizawa, Effect of alloying elements on stability of epsilon iron, Trans. Japan Inst. Met. 15 (1974) 225–231.
[43] A. Fossati, F. Borgioli, E. Galvanetto, T. Bacci, Glow-discharge nitriding of AISI 316L austenitic stainless steel: influence of treatment time, Surf. Coat. Technol. 200 (2006) 3511–3517, https://doi.org/10.1016/j.surfcoat.2004.10.122.
[44] A. Fossati, F. Borgioli, E. Galvanetto, T. Bacci, Corrosion resistance properties of glow-discharge nitrided AISI 316L austenitic stainless steel in NaCl solutions, Corros. Sci. 48 (2006) 1513–1527, https://doi.org/10.1016/j.corsci.2005.06.006.
[45] M.K. Lei, Z.L. Zhang, X.M. Zhu, Effects of nitrogen-induced hcp martensite formation on corrosion resistance of plasma source ion nitrided austenitic stainless steel, J. Mater. Sci. Lett. 18 (1999) 1537–1538.
[46] F. Borgioli, E. Galvanetto, T. Bacci, Surface modification of a nickel-free austenitic stainless steel by low-temperature nitriding, Metals 11 (2021) 1845, https://doi.org/10.3390/met11111845.